applied sciences

MDPI

Article

Additive Manufacturing Oriented Parametric Design Automation of Adaptive Joint System for an Irregular Form Gridshell Structure

Jin-Ho Ahn [1], Nam-Hyuk Ham [2,*], Ju-Hyung Kim [1] and Jae-Jun Kim [1]

[1] Department of Architectural Engineering, Hanyang University, Seoul 04763, Republic of Korea; endeinc@hanyang.ac.kr (J.-H.A.); kcr97jhk@hanyang.ac.kr (J.-H.K.); jjkim@hanyang.ac.kr (J.-J.K.)
[2] Department of Digital Architecture and Urban Engineering, Hanyang Cyber University, Seoul 04763, Republic of Korea
* Correspondence: nhham@hycu.ac.kr

Abstract: In architectural engineering, triangular tessellation using polygon mesh topology is one of the commonly used computational geometric approaches to simplify a free curved building façade into flat triangular facets and their subsequent straight edges. In such a façade system, exterior panels are supported by a network of profiles that correspond to their edges hidden behind the panels at an offset distance. A group of profiles, derived from the edges common to a node point of tessellated panels (i.e., the outermost panels enveloping the building), may dislocate from each other when offset from their original locations due to non-coplanar alignment and unique offset directions and distances. This dislocation problem gives rise to geometric complications in nodal connector design in addition to varying in the connected profile count and orientations. Design considerations regarding the effects of 'offset vertex dislocation' (i.e., the dislocation of the edges when it offsets from the original topology due to incoherent normal direction) should incorporate proper variables in the correct sequence based on a fundamental understanding that causes the dislocation problem. However, it is very often these topological problems pertaining to offset that are neglected, leading to subsequent design flaws. Such oversights diminish the inherent strengths of DfMA (design for manufacture and assembly) and design automation. This study develops a computational mathematical approach aimed at addressing the geometric complexities in nodal connector design. It focuses on two main areas: the precise positioning of substructure profiles essential for the design and a design automation approach that minimizes the length of the nodal connector arms to enhance 3D printing productivity. A life-scale proof-of-concept structure based on an automated parametric design process that implements the research findings demonstrates the application, incorporating 3D-printed PA12 (Polyamide-12) nodal connectors.

Keywords: nodal connector; gridshell structure; design automation; parametric design; additive manufacturing; DfMA

Citation: Ahn, J.-H.; Ham, N.-H.; Kim, J.-H.; Kim, J.-J. Additive Manufacturing Oriented Parametric Design Automation of Adaptive Joint System for an Irregular Form Gridshell Structure. *Appl. Sci.* **2024**, *14*, 11038. https://doi.org/10.3390/app142311038

Academic Editors: Sangjin Jung and Giangiacomo Minak

Received: 14 October 2024
Revised: 3 November 2024
Accepted: 16 November 2024
Published: 27 November 2024

1. Introduction

The development of computational design technology and the introduction of digital manufacturing methods have been the foundation for the advancement of irregular-shaped architecture [1]. The recent emergence of new digital manufacturing technologies, including AM (additive manufacturing), has shown new design possibilities [2]. Parametric design tools and AM technology provide increased capabilities in design and manufacturing, especially when dealing with complex shapes [3].

Parametric design is a design paradigm that distinguishes it from traditional design processes using CAD and uses a differential geometric approach [4] to create an automated modeling process where design decisions are made by algorithms instead of relying on the designer's arbitrary judgment. Using parametric tools, a designer can effectively perform

precise numerical control over complex shapes [5] such as curves and surfaces on repetitive and complex design tasks.

An irregularly shaped gridshell façade is composed of parts that are repeated but not identical to one another. While each part follows the same design procedure, the local geometric constraints of irregular structures are interdependent with the surrounding geometric context [6]. Therefore, the conventional design method relying solely on manual design poses many problems, particularly in relation to human error. The parametric design ensures efficiency and reliability in such circumstances.

The process and methodology of parametric design should be designed to ensure quantitative criteria for decision-making in every aspect, unlike design using CAD, where the designer can intervene based on their judgment at any given moment [7]. Therefore, an algorithm with proper constraints should be established for each step of the process based on an understanding of the design constraints.

Nodal joints in irregular-shaped gridshell structures must satisfy many constraints, and the resulting complex shapes pose many challenges in terms of fabrication [6]. Designing a nodal joint that satisfies many degrees of freedom with limited fabrication methods is very difficult and can lead to complex shapes and increased assembly parts. This problem is also associated with increased production costs and a decreased reliability of components, as well as aesthetic issues. In some cases, to alleviate complexity issues, only a limited range of degrees of freedom [8,9] is secured or, even worse, omitted, which can reduce the design freedom of the shape being implemented and diminution of construction precision [10,11].

AM technology has made significant progress since its inception and is distinguished by its ability to replicate precise and intricate shapes that have posed challenges for other fabrication methods, such as a multi-axis CNC (computer numerical control) machining center. Also, previously recognized drawbacks of AM methods, such as low productivity, high costs, and a limited spectrum of material choices, are being overcome. Through design for manufacturing and assembly (DfMA), significant improvements have been made not only in the performance of AM products but also in productivity and cost aspects. With parts integration and uni-body designs, AM parts demonstrate better constructability and higher structural integrity compared to the previous iterations.

This study proposes a novel design approach that addresses the complex and impractical designs resulting from the limited manufacturing methods of conventional nodal connectors, using the AM production method and parametric design automation. Firstly, the geometric constraints required for irregular-shaped curtain wall facades were identified, and mathematical implementations were established. Secondly, a complete automated design algorithm was developed based on the mathematical approach for automatic optimization of the connector arm length, which previously required the designer to interrupt the automation process to manually intervene with shape control. The nodal connector was designed taking into consideration the characteristics of the AM production method and DfMA for construction efficiency. To validate the design, an actual structure was fabricated.

2. Materials and Methods

2.1. Parametric Design Automation

Traditional design approaches that rely on a designer's intuition and judgment to satisfy multiple geometric variables simultaneously in a complex shape have limitations since these variables have complex correlations with one another [12]. In contrast, the parametric design approach iterates through an algorithm with a specified shaping procedure based on the correlations between each variable [1]. In case the procedure is simple enough, the correlation pattern between the resulting shape and input parameters may well be intuitively understood and predictable to a certain extent; if the procedural complexity arises, such a clear pattern starts to diminish [1]. In parametric design, the designer only specifies the relationships between variables and the shaping procedure and does not directly interfere with the shaping process [12]. This feature enables an effective design

process regardless of the complexity or diversity of the design, and particularly, it allows for rational and accurate results that fully reflect the design intention.

Parametric design algorithms have a particular strength in dealing with designs that require implementing the same design procedure over different geometric conditions. Especially in irregular-shaped designs, where parts with different conditions must be immediately reflected in the results regardless of quantity or condition, the efficiency of the design is greatly increased through automation. Furthermore, parametric design algorithms can effectively respond to changes in initial variables or design conditions [13].

Shape control in parametric design, especially pertaining to NURBS (non-uniform rational B-splines) geometry, has its mathematical foundations in differential geometry [4,5], and control of curve and surface generation, transformation, and other operations are carried out through this method.

Most modeling software provides a mouse input interface in addition to a numeric input interface that is preferred by the majority of the users for its visual intuitiveness and easier control. This approach is particularly preferred for controlling the curved surfaces and this remains the standard paradigm in 3D design software. This is one of the biggest issues in the parametric design process, where all aspects of the design must be controlled quantitatively. In parametric design, the designer only defines the algorithm [5,7] and cannot interfere with the algorithm in the middle of the process. For example, the condition 'select similar shapes nearby' may seem unambiguous to designers, but from the algorithm's perspective, a specific and mathematically clear method must be sought out.

The parametric algorithm that replicates the empirical procedure of manual modeling is often preferred for its intuitiveness, but it is not always an effective method. In contrast to manual modeling, in parametric modeling, rich geometric information can be utilized to seek more effective methods than manual modeling procedures. In addition, to alleviate the high computational load in parametric design, an efficient method may also be necessary.

2.2. Design Considerations in DfMA of AM Parts

Contrasting from the subtractive manufacturing method (retronym for machining processes that sculpts a form by removing material from the initial block material), AM, in general, does not suffer from the sculpting of hollowed-out shapes and undercut issues usually reserved by subtractive manufacturing methods [6,14]. Also, those 3D-printing technologies that do not require support structures on printing parts, such as PBF (power bed fusion) and BJ (binder jet) allow parts stacking on a single build volume for added productivity both on time and costs [15].

In AM, measures are taken to maximize the packing density within the job box (i.e., the space within the 3D printer where the actual printing process occurs) to enhance productivity. Packing density is affected by various factors, such as the shape and size of the objects. From a design perspective, protruding parts and unnecessary details are the main factors that decrease the packing density, which should be considered in the design stage. Also, unlike subtractive manufacturing, the anisotropic property of additive manufacturing requires printing orientations to be considered [3,16], especially when structural performance matters [17]. The PBF 3D-printing process generates a lot of heat, and parts may undergo thermal deformation [18] in the printing and cooling process, depending on the shape of the parts. For instance, parts with uneven thicknesses are more susceptible to heat deformation due to uneven shrinkage in the cooling stage [19]. The productivity of additive manufacturing is influenced more by the size and amount of material used rather than the complexity of the shape. Therefore, methods such as topology optimization to minimize material can be effective on 3D-printed parts [20].

Additive manufacturing has superior aspects in terms of formability compared to the subtractive machining process. While the formability of CNC is affected by the freedom of the axis, which makes it hard to carve out undercuts and hollow shapes, additive manufacturing is relatively free from such constraints [21]. Additionally, unlike subtractive machining, where material consumption and processing time are heavily affected by the

complexity of the shape, additive manufacturing allows efficient shaping without being constrained by the shape. Parts that would need to be made separately using subtractive machining can be designed as uni-body shapes, enabling proactive consideration of DfMA (design for manufacturing and assembly) [22].

While CNC can handle almost any solid material that can be machined, the material choice in additive manufacturing is relatively limited. The spectrum of material choice becomes even narrower depending on the choices of 3D-printing technology. Anisotropic properties due to defective layer adhesion problems [3,16] and the reluctant choice of low melting point materials in the case of FDM (fused deposition modeling) to ensure an adequate flow during the extrusion and sintering efficiency in the SLS (selective laser sintering) process pose performance issues of the parts made via the AM method. However, adaptation of high-performance polymers such as PA12 (Polyamide-12) and metal-reinforced polymer composite materials can secure higher structural performance [23], and 3D-printing technologies that can print parts with characteristics close to isotropic are being developed to mitigate material performance issues in the additive manufacturing process [17].

2.3. DfMA of Irregular-Shaped Gridshell Structure

It is a basic principle of mass manufacturing that the production cost and batch size are in an inverse relationship [24]. Such an effect is emphasized under circumstances where the batch size is large enough to take advantage of mass production [24], which is the case of the regular-shaped gridshell façade system that covers a large building envelope. The problem arises when each nodal connector has different geometric conditions; to maintain production costs at its minimum, certain DfM (design for manufacturing) strategies should be considered [25]. Such a DfM strategy in the design stage includes the minimization of one-of-a-kind parts in connector assembly with maximized identical parts that are common amongst each connector. Another DfM challenge arises when added complexity in nodal connector design due to higher design freedom [10,11] entails a subsequent increase in assembly parts, which makes it very hard to maintain the assembly parts count to a minimum. Considering production costs, limited modes of manufacturing due to complex shaped parts [26] and an increased parts count in assembly leads to higher production costs and reduced reliability of the assembled components.

3. Problem Statement

3.1. Multiple Degrees of Freedom in Irregular-Shaped Gridshell Structure Connector Design

In grid shell structures, a nodal connector design should implement multiple axes of freedom (Figure 1) consisting of multiple rotations and linear movements [11,13]. Even with small changes in the parameters, such as the dimensions of a profile's cross-section or panel thickness, the effect does not remain local; instead, the effect propagates through the entire structure. Therefore, it is necessary to understand the geometric causality of the elements of the structure. Based on this causality, at each sequentially arranged stage, mathematical approaches to determine the exact amounts of motion for linear and rotational transformations are required. Therefore, constructing an automated design process is essential for an efficient design.

3.2. Vertex Normal Dependent Connector Design

In a gridshell structure, a nodal connector is used to connect the surrounding profiles onto a common vertex point [27]. For ease of fabrication, nodal connectors usually accompany the details that are fanning around a single axis of rotation (a vertex normal vector in many cases) like the case shown in Figure 2. Because profiles fanning around a node are not coplanar in irregularly shaped triangular tessellated envelopes, profiles intersect with their adjacent counterparts in an unpredictable manner. To alleviate this problem, a planar contact plate is inserted between the profiles near the node, accommodating sufficient

contact surface for both profiles. The size and shape of these flanges are different from one another, depending on the cross-sectional union boundary between the profiles.

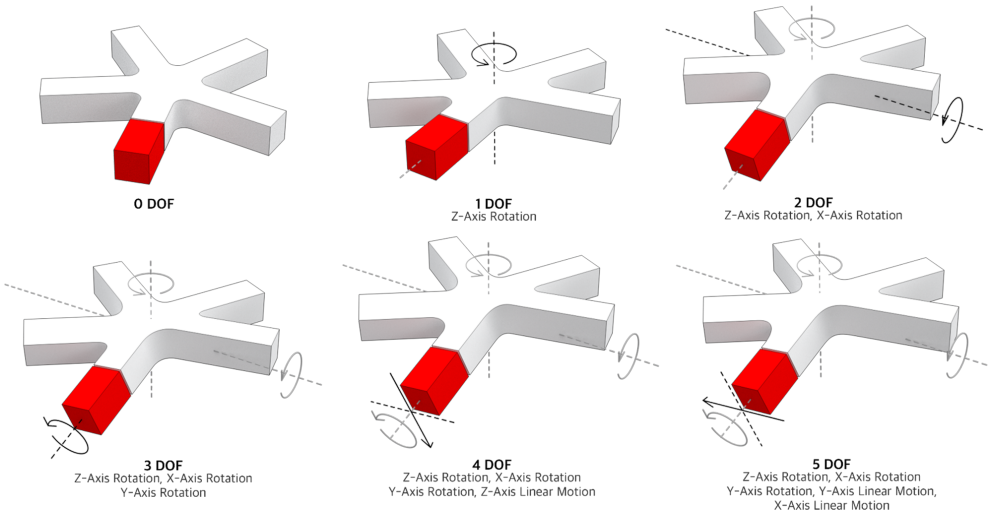

Figure 1. Multiple degrees of freedom of connectors used to join the members of the structure to accommodate the complex geometry.

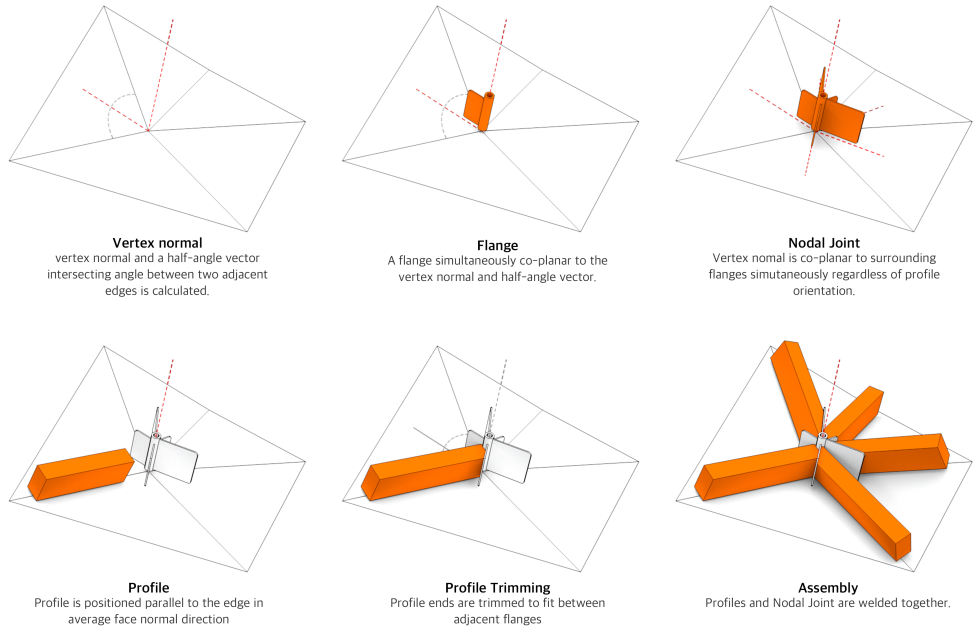

Figure 2. Design process of widely used flanged nodal connectors.

Each end of the profile is uniquely trimmed using a pipe laser to fit between the two adjacent flanges for a maximized welding length (Figure 3).

In a gridshell façade system, each element can be assumed as part of a mesh surface network [28]. In a mesh network, the dimensional error of a single element in the mesh is passed on to one another, affecting nearby elements to deviate from their correct position. Assuming other elements are in the correct dimension, this effect is maintained locally. If the dimensional error is prevalent in the manufacturing process, the effect of deviation is not localized and would cumulate across the mesh network, causing a large number of elements to deviate beyond its acceptable tolerance boundary.

While the dimensional error of profiles can be well maintained to an acceptable range using digital fabrication technology, several factors in the manufacturing and assembly process may tarnish the efforts [29]. For instance, a misaligned angle between each contact plate or welding position between the profile and nodal connector in the manual welding

process affects the distance between adjacent vertices to deviate from their position. It is these unreliable manual works that cumulate errors in each manufacturing and assembly process [29].

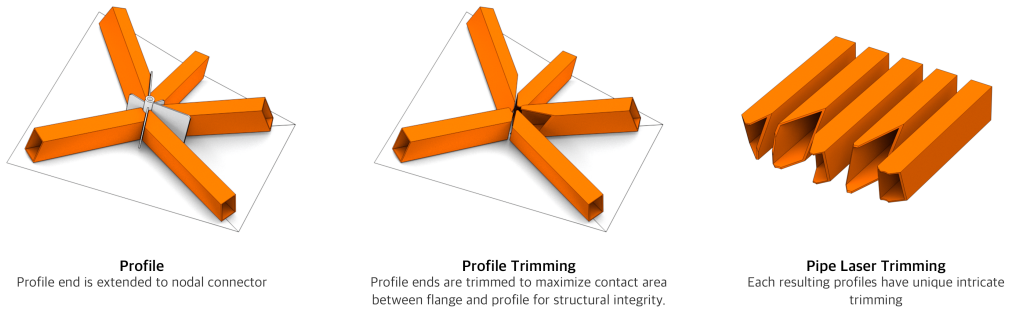

Figure 3. Laser trimming at the ends of the profiles for welding.

3.3. Edge Normal Vector in Polygon Mesh Topology

Figure 4 shows the relationship between face normal, edge normal, and vertex normal.

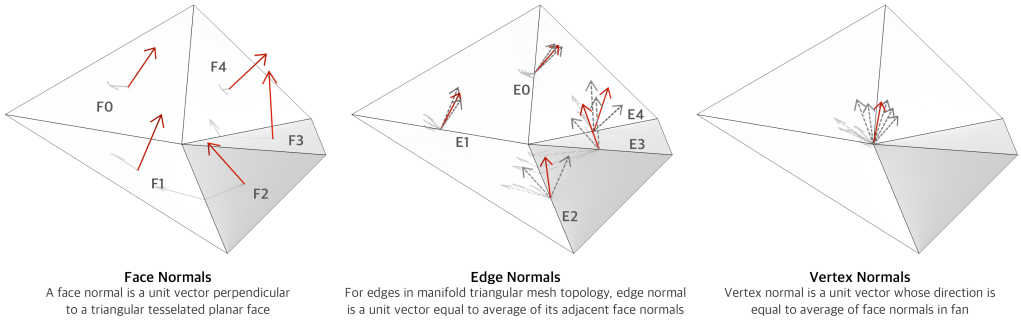

Figure 4. Interrelated relationship between face normal, edge normal and vertex normal shows how local alteration propagates through adjacent structure.

Given that vectors $\vec{V}_A$, $\vec{V}_B$, and $\vec{V}_C$ each represent the position vector of vertices on the face F, the face normal vector $\vec{N}_F$, which is perpendicular to both $\vec{V}_{B-A}$ and $\vec{V}_{C-A}$, is obtained using the cross product of these two vectors.

$$\vec{N}_F = (\vec{V}_B - \vec{V}_A) \times (\vec{V}_C - \vec{V}_A) \tag{1}$$

In general, 'edge normal' is not defined in computational mesh geometry. However, in this research, the edge normal $\vec{N}_{E_i}$ of edge E_i is defined as a vector dissecting the folding angle between the two adjacent faces into half. Given that the face normal of each face F_i and F_{i+1} are $\vec{N}_{F_i}$ and $\vec{N}_{F_{i+1}}$ respectively, the edge normal $\vec{N}_{E_i}$ is:

$$\vec{N}_{E_i} = \vec{N}_{F_i} + \vec{N}_{F_{i+1}} \tag{2}$$

Vertex normal is an average of the face normal of the faces fanning around a vertex [30,31]. In computer graphics, the average can be weighted by the surface area for rendering purposes [32], but in this research, the average is unweighted.

3.4. Vertex Dislocation Problem

Each profile in a gridshell curtain wall structure has a unique offsetting distance and direction (edge vector) from its referenced edge in the mesh surface, as shown in Figure 4. The direction of the offset $\vec{N}_E$ is set to bisect the angle formed by the two surfaces facing the edge of the panel surface, and the offset distance is determined by the folding angle of the surfaces at the edge. Offsetting of the profile center line is unavoidable as long as the

profile has a cross-section dimension. This leads to the dislocation of edges from a common converging point as they move away from the mesh surface (Figure 5b). Profile center lines maintain converging to a point only if the folding angle of the panels is consistent, as shown in Figure 5a.

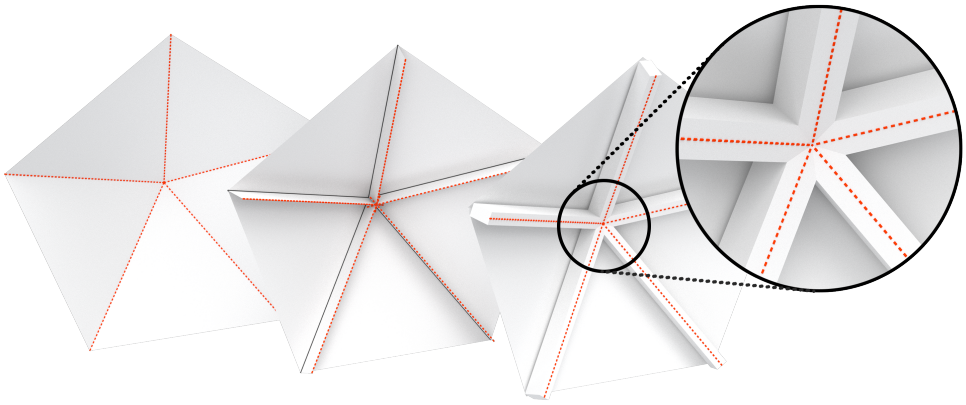

(**a**) Edges converge to a point regardless of offset distance if the folding angle of the panels in the fan is consistent.

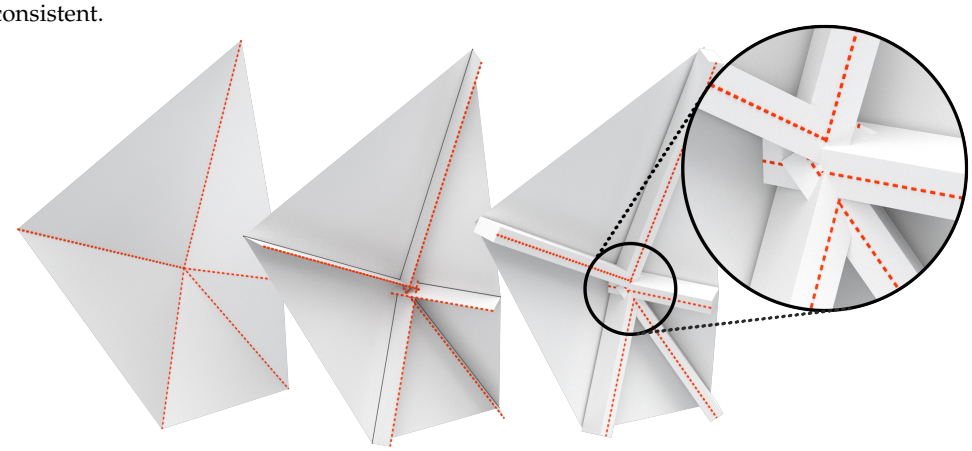

(**b**) Edges dislocate from each other if the folding angle of the panels in the fan are varied.

Figure 5. Vertex dislocation problem.

Except for regular shapes like platonic solid shapes, profiles fanning around a node have different offset directions and distances, and therefore, the edges that were coincident at the node will diverge into different directions as they depart from the node, hence the term 'Vertex Dislocation Problem' (Figure 5b). Therefore, design approaches that assume a hypothetical common axis of reference, as shown in the cases of Figures 2 and 6a, cannot be generalized. Figure 6b, although the use of different thickness tapered shim on each side of the profile hinge adds additional freedom to the profile to shift left and right and rotate around the directional axis of the profile, it cannot be applied in the case of extreme conditions where dislocation exceeds the allowed margin.

A type of nodal connector, as shown in Figure 6a, can only be applied in cases with regular shapes, including those involving a platonic solid, for instance. If, as in Figure 7, the offset trajectory vector of the profile $\vec{N}_{E_i}$, the edge directional vector $\vec{N}_{E_i}$, and the central axis vector of the nodal connector $\vec{N}_V$ are on the coincidental plane, the following condition should be satisfied:

Utilizing the volume of a parallelepiped of three vectors by scalar triple product, if vectors $\vec{N}_V$, $\vec{N}_{E_i}$, and $\vec{V}_{E_i}$ are coplanar (Figure 6a):

$$\vec{N}_{E_i} \cdot (\vec{N}_V \times \vec{V}_{E_i}) = 0 \tag{3}$$

Because Equations (2) and (3),

$$(\vec{N}_{F_i} + \vec{N}_{F_{i+1}}) \cdot (\vec{N}_V \times \vec{V}_{E_i}) = 0 \tag{4}$$

$$\vec{N}_{F_i} \cdot (\vec{N}_V \times \vec{V}_{E_i}) = -\vec{N}_{F_{i+1}} \cdot (\vec{N}_V \times \vec{V}_{E_i}), \tag{5}$$

where $\vec{N}_V \times \vec{V}_{E_i}$ is a vector in the same direction of the profile plane X-axis

$$|\vec{N}_{F_i}| \cdot |\vec{N}_V \times \vec{V}_{E_i}| \cdot \cos\theta_{F_i} = -|\vec{N}_{F_{i+1}}| \cdot |\vec{N}_V \times \vec{V}_{E_i}| \cdot \cos\theta_{F_{i+1}} \tag{6}$$

where θ_{F_i} is the angle between $\vec{N}_V \times \vec{V}_{E_i}$ and $\vec{N}_{F_i}$; $\theta_{F_{i+1}}$ is the angle between $\vec{N}_V \times \vec{V}_{E_i}$ and $\vec{N}_{F_{i+1}}$ (Figure 8)

$$\cos\theta_{F_i} = -\cos\theta_{F_{i+1}} \tag{7}$$

$$\theta_{F_i} = \pi - \theta_{F_{i+1}} \tag{8}$$

This is the case when both faces form the same angle with respect to the plane made by $\vec{N}_V$ and $\vec{N}_{E_i}$. Therefore, except for special cases, a nodal connector like the one shown in Figure 6a cannot be used in an irregularly shaped gridshell system. Figure 6b depicts a type of nodal connector that allows slight axial rotation of the profile using a silicon shim [33]. This detail accommodates a limited margin of torsion tolerance around the central axis of the profile but cannot be used in extreme conditions.

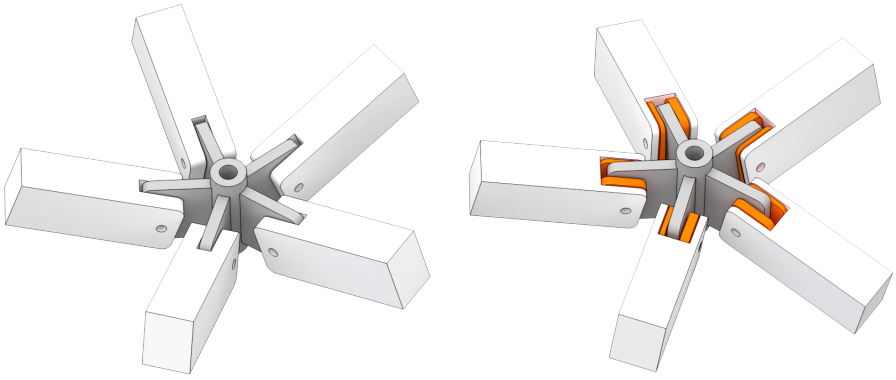

(**a**) (**b**)

Figure 6. Examples of vertex normal dependent nodal connector designs. (**a**) A nodal connector with 4 axes of freedom ($\vec{N}_V$, $\vec{N}_{E_i}$, and $\vec{V}_{E_i}$ are coplanar); (**b**) A nodal connector with 5 axes of freedom, using tapered shims ($\vec{N}_V$, $\vec{N}_{E_i}$, and $\vec{V}_{E_i}$ are not coplanar).

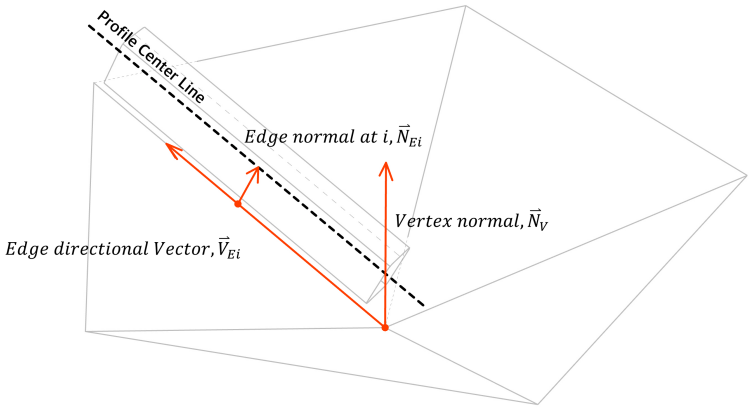

Figure 7. Offset trajectory vector of the profile $\vec{N}_{E_i}$, edge directional vector $\vec{N}_{E_i}$, and the central axis vector of the nodal connector $\vec{N}_V$.

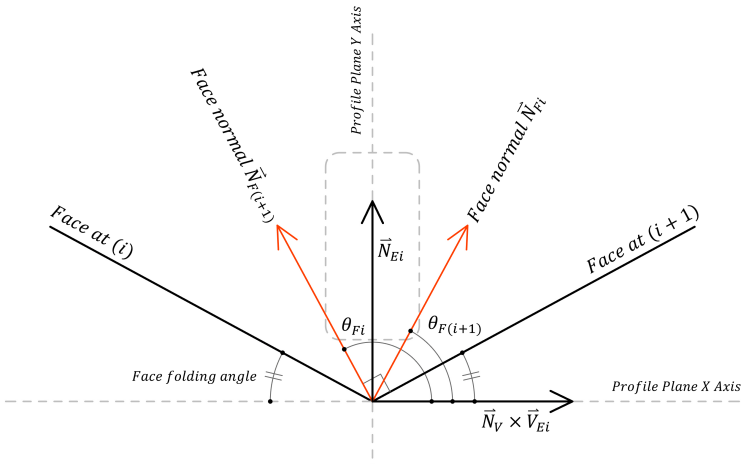

Figure 8. Projection of $\vec{N}_{F_i}$ and $\vec{N}_{E_i}$ to a plane perpendicular to $\vec{V}_{E_i}$.

4. Parametric Design Automation

4.1. Sequential Order of Profile Orientation in Irregular-Shaped Gridshell Structure

The design of the nodal connector incorporates complexities arising from the non-uniform edge normal. Therefore, a design capable of securing multiple degrees of freedom is required. The final form of the connector is influenced by multiple variables, including the profile cross-section shape, as previously mentioned. More importantly, the condition and shape change in one part influence the orientation and shape of the neighboring components. Many variables affecting the design of the gridshell structure form complex mathematical correlations and hierarchical dependencies, and the establishment of the hierarchy and relationship of these variables is necessary for an automated design.

Figure 9 shows the procedural process of the profile's offset displacement vector and the shaping of the nodal connector. The profile geometry does not act as a direct variable in this process but determines its position through the transformation of the coordination frame that controls the profile's orientation. Each profile geometry connected to a common nodal connector is assigned a unique coordination frame, and their final positions are determined through the transformation process outlined in Figure 9.

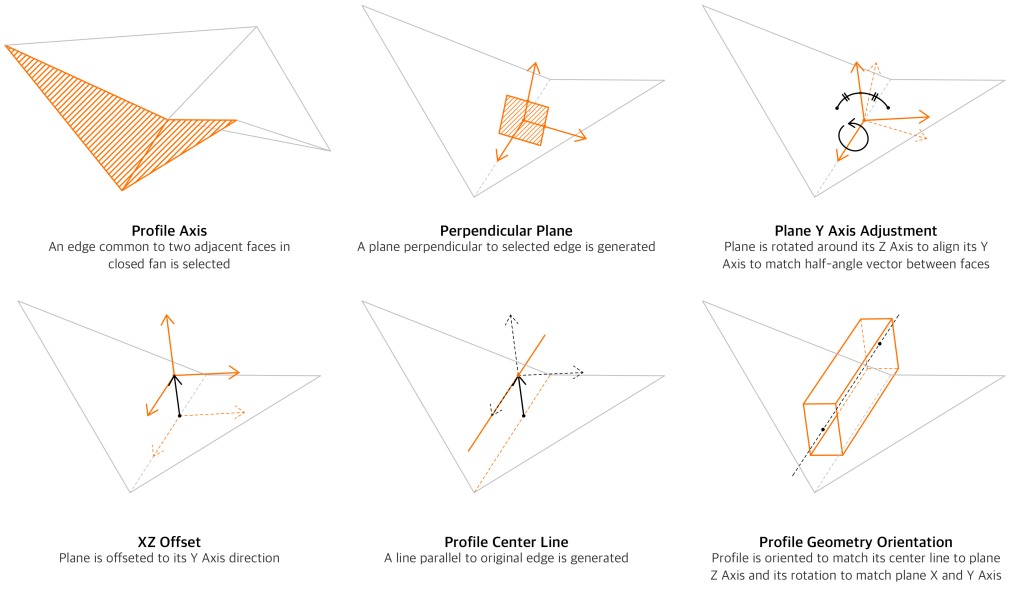

Figure 9. Profile orientation process in sequential order.

The profile is a structural component that supports the panels of the gridshell, and the orientation of the profile geometry is subsequent to the two panel faces common to the edge.

Meanwhile, the nodal connector is dependent on all the profiles connected to the node. Therefore, the shape of the nodal connector cannot be finalized until the positioning of the profiles is determined. Consequently, the shaping of the nodal connector is procedurally subsequent to the profile geometry, and the design of the profile must precede (Figure 10).

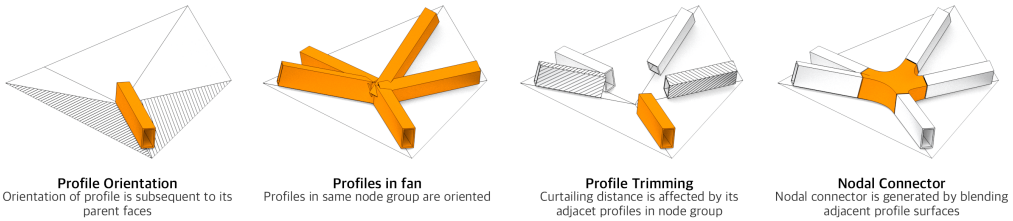

Figure 10. Design of nodal connector precedes profile orientation process.

4.2. Profile Base-Plane

In mathematics, the general representation of a plane in $\mathbb{R}^3$ is as follows:

$$ax + by + cz + d = 0 \tag{9}$$

The normal vector $\vec{N}$ can be identified directly from the coefficients of x, y, and z as follows:

$$\vec{N} = (a, b, c) \tag{10}$$

In computational geometry, a coordinate frame is used to effectively control the orientation of geometry. In this case, a plane is considered as a Cartesian coordinate system with an identifiable origin point and the X-, Y-, and Z-axes in vector form, which the above mathematical representation does not expose (Figure 11a).

Figure 11a shows the properties exposed by the plane. In 3D space, the position and orientation of a geometry object are defined by the base plane. In computer graphics, the orientation of a geometric object in 3D space is calculated using a plane-to-plane transform matrix. The final position of the profile is determined through the movement and rotation of the locally defined plane (Figure 11b). Here, the local plane of the profile (profile plane) takes the center of the base geometry as the plane's origin, and the profile geometry's Z-axis and Y-axis are defined to align with the profile's extrusion direction and the direction facing the panel edge, respectively (Figure 11b).

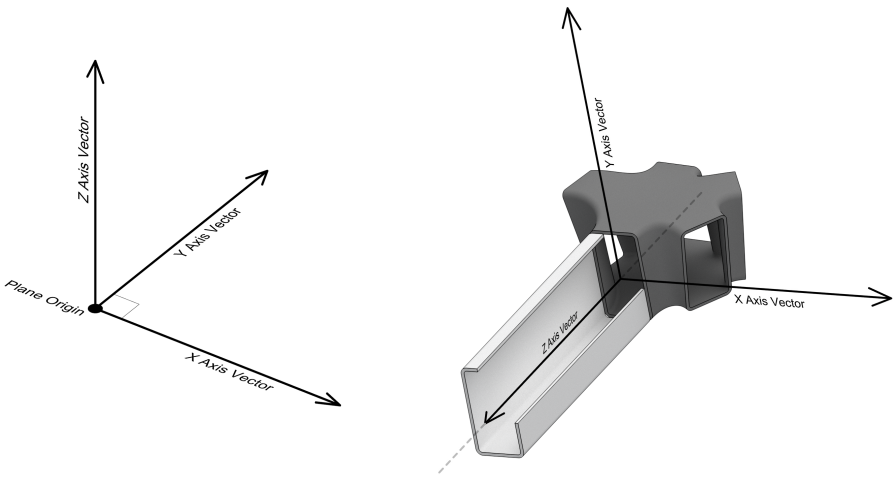

(**a**) (**b**)

Figure 11. Plane class in computer graphics. (**a**) Graphic visualization of plane class properties; (**b**) Profile base plane.

4.3. Profile Z-Axis Offset Distance

Figure 12 illustrates the profile detail supporting two panels that meet at the edge. The distance between the central axis of the profile and the edge of the panel surface increases as the dihedral angle of the panel decreases. If the distance between the panel edge and the central axis of the profile is set to be equal regardless of the dihedral angle in pursuit of a simplified nodal connector design, the connection detail between the profile and panel must be individually considered to maintain the panel at its location. However, even in this case, there is no elimination in the number of axial degrees of freedom required for the nodal connector, so there is no benefit in terms of manufacturing and design. Rather, the increase in the parts that must be individually manufactured would increase the cost. Therefore, the design should be done in a way that maintains the same profile section detail regardless of the dihedral angle by varying the offset distance.

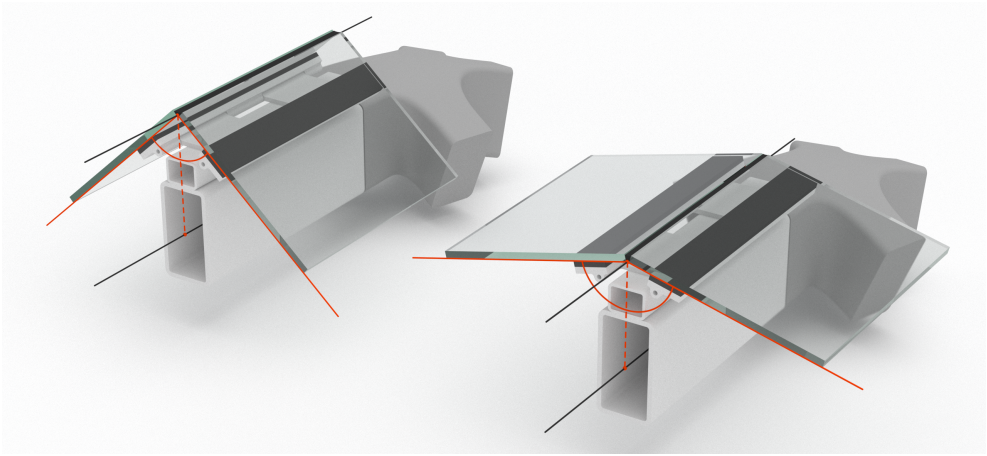

Figure 12. Cutaway section of profile detail supporting glass panels with different folding angle.

The distance between the profile center line (profile plane Z-axis) and the panel edge (Figure 13) takes several variables as its parameters. Define D_p as the Y-axis aligned distance from the profile center line to the pivot points, D_o as the perpendicular distance from the panel to the pivot point, D_s as the spreading distance between two pivot points, and θ as the folding angle, and then H_1 and H_2 is calculated as follows:

$$H_1 = \frac{D_o}{\sin\left(\frac{\theta}{2}\right)}, \quad H_2 = \frac{D_s}{2\tan\left(\frac{\theta}{2}\right)} \quad (-\pi < \theta < \pi) \tag{11}$$

Therefore, the offset distance D_{Offset} is:

$$D_{\text{Offset}} = H_1 + H_2 + D_p = \frac{D_o}{\sin\left(\frac{\theta}{2}\right)} + \frac{D_s}{2\tan\left(\frac{\theta}{2}\right)} + D_p \tag{12}$$

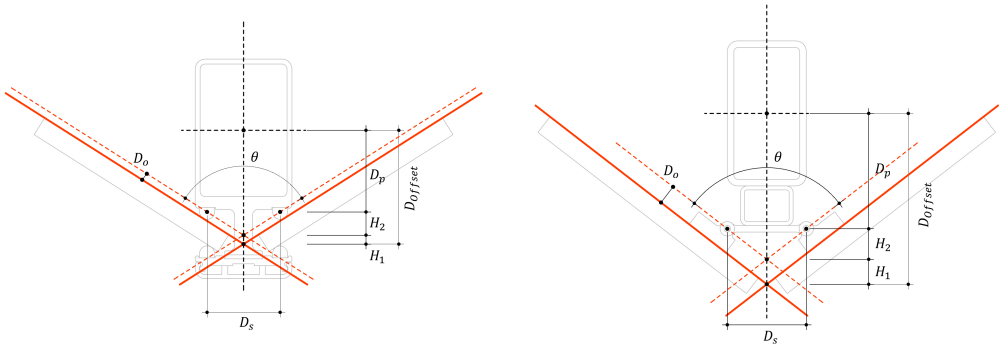

Figure 13. Profile offset distance and dihedral angle on different support detail.

Notice that the panel baseline is set to face inward, in contact with the saddle. This design choice is made to maintain the interior volume close to its original model.

It is important to notice that the panels always pivot around the pivot point at a distance D_o. Failure to consider this will leave a gap between panels. Additionally, in cases where the center of the pivot is not stationary (Figure 14), D_o and D_s should also be treated as angle-dependent variables.

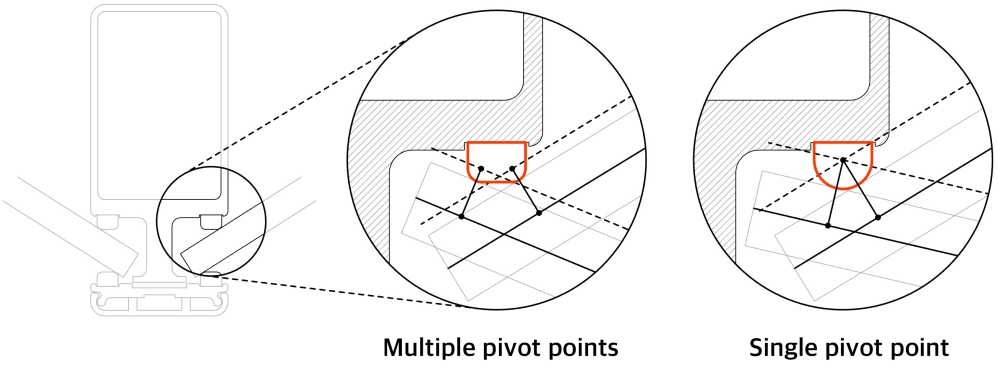

Figure 14. Panel pivot point.

The implementation of this process in Rhino C# script is shown in Listing 1. This function replicates the sequential procedure presented in Figure 9, using Equation (12) to determine the profile offset distance.

Listing 1. Profile base-plane offset calculation.

```
private void RunScript(
double Dp,
double Ds,
double Do,
Brep faceA,
Brep faceB,
Point3d vertexPt,
ref object a)
{
  //Face normals of Face A and Face B
  Vector3d faceNormalA = faceA.Faces[0].NormalAt(0.5,0.5);
  Vector3d faceNormalB = faceB.Faces[0].NormalAt(0.5,0.5);

  //Profile Frame Z Axis vector (zAxis) from cross product between surface normal of FaceA and FaceB
  Vector3d zAxis = Vector3d.CrossProduct(faceNormalA,faceNormalB);

  //Profile Frame −Y Axis (edgeNormal) from average of surface normal of FaceA and FaceB
  Vector3d edgeNormal = faceNormalA + faceNormalB;
  edgeNormal.Unitize();

  //Profile Frame X Axis (xAxis) from rotating Y Axis vector 90 degrees around Z Axis
  Vector3d xAxis = new Vector3d(−edgeNormal);
  xAxis.Rotate(Math.PI/2,zAxis);

  //Get profile offset distance (dOffset)
  double foldingAngle = Math.PI−2*Math.Acos(faceNormalA*edgeNormal);
  double h1 = Do/Math.Sin(foldingAngle/2);
  double h2 = Ds/(2*Math.Tan(foldingAngle/2));
  double dOffset = h1 + h2 + Dp;

  //Construct profile base frame
  Plane profileFrame = new Plane(vertexPt+edgeNormal*dOffset,xAxis,−edgeNormal);

  a = profileFrame;
}
```

4.4. Automating Minimum Protruding Connector Arm

The nodal connector is a core element of the gridshell curtain wall, anchoring the positions of these profiles that do not meet at an exact point to provide structural integrity.

The type of nodal connector shaped as shown in Figure 10 that blends surrounding profile shapes can easily adapt to complicated geometric settings where profiles converging from different directions have discrete offset directions and rotation angles (Figure 9). While aesthetically beautiful and structurally superior, manufacturing such an intricate part has been a challenge both in economic and technological aspects. However, with the advancement of AM technology, the cost and technical issues related to complex shapes are being alleviated due to AM's high degree of shaping freedom and rapid speed.

The size of the nodal connector is directly related to the production time and the job box packing density, which are the largest factors affecting manufacturing costs and time. Therefore, the size of the nodal connector must be kept to a minimum. The connector arm is the part protruding from the nodal connector that connects the nodal connector to the profile. The volume of the nodal connector is mainly influenced by the protrusion length of the connector arm, and the arm's length must be restricted as much as possible to minimize the volume of the nodal connector. The protrusion distance of the connector arm must be set to the minimum distance required to avoid interference between the two profiles adjacent to the corresponding profile on both sides. This length cannot be uniformly applied, as it varies depending on the angle formed by the two profiles adjacent to the corresponding profile. This part has so far been determined by the designer's visual sense, which inherently costs a lot of time in the design process and negatively affects the automated design process. Therefore, mathematical methods must be considered for the automatic optimization of the arm length.

Figure 15 is a simplified 2D diagram depicting the process of determining the minimum arm length.

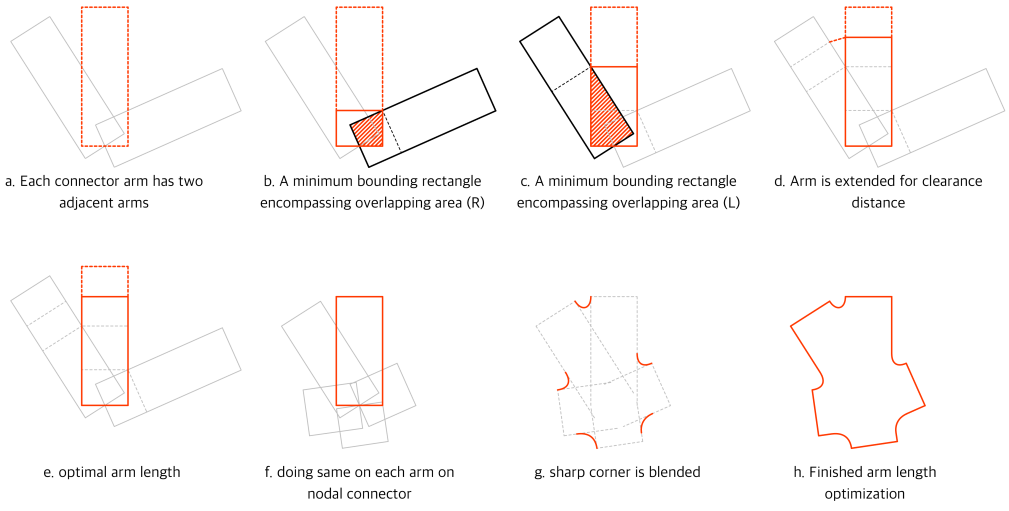

Figure 15. A 2D depiction of minimum arm length finding process.

Every profile connected to the nodal connector has two neighboring profiles on either side. For each neighboring profile, there exist two minimum arm lengths to avoid interference between the profiles. Since both conditions must be met simultaneously, the larger of the two values is taken. In 2D, this can be easily determined using trigonometry, but in 3D, more factors are taken into account as the central axes of the profiles do not intersect, and the rotation of the profiles about their central axes would yield different intersecting outcomes (Figure 16).

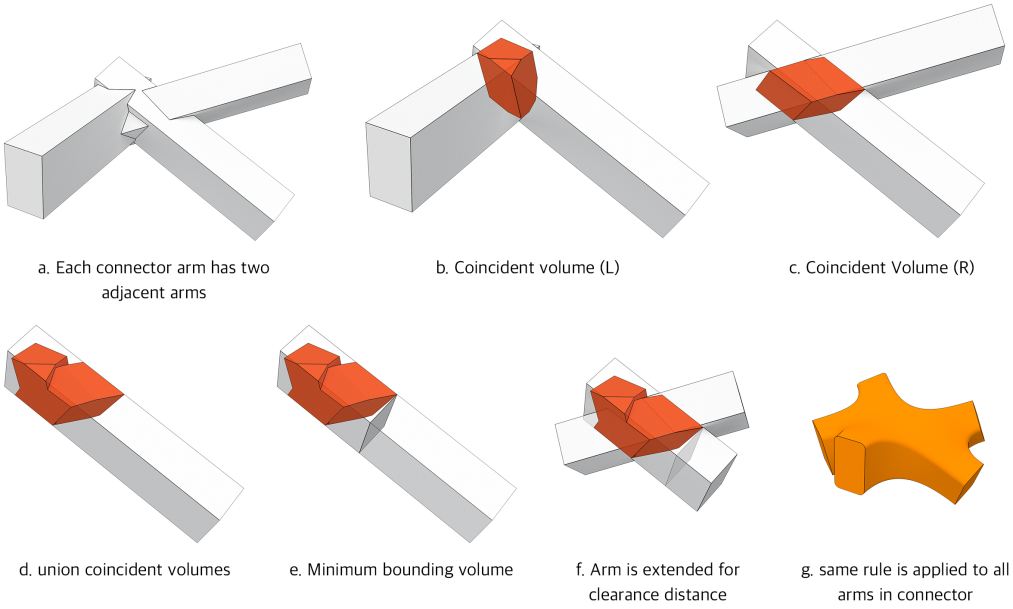

Figure 16. Minimum arm length using volumetric Boolean shape.

Two approaches, geometric and mathematical, were devised to determine the optimal arm length. The first method, as illustrated in Figure 16, uses a minimum bounding box (i.e., a box with the smallest volume within which the convex-hull of captive geometry lie [34,35]) of an intersecting volume between the profiles to find the minimum arm length. In contrast, the second method calculates the points that form the minimum distance between two non-intersecting straight lines. The former can provide accurate results through a simple process but requires a considerable computation load for volumetric Boolean operations. In contrast, the latter offers a faster computational speed but might result in a slightly larger volume due to assumptions incorporated into the calculation.

Every arm of the node has neighboring arms on either side, and the arm length must be set to a length that does not interfere with both neighboring arms. The minimum arm length can be determined by the height of the bounding box that encloses the intersecting volume of the adjacent two arms. Since interference must be considered for the profiles located on either side, volumetric Boolean operations are needed for each of the arms on both sides. To minimize the time required for Boolean operations, the profile is assumed as a minimum bounding box of the profile with respect to the profile plane. The larger of the height values obtained from the bounding boxes for each of the left and right profiles is taken and designated as the minimum arm length. Listing 2 shows Rhino C# script to replicate the process of Figure 16 to figure out the minimum arm length.

Each profile's center line offsets from the panel edge in a different direction and distance, which causes them to fall apart from the common node point. However, the displacement distance of the center axes is mostly influenced by the dihedral angle; therefore, as long as the dihedral angle is maintained close to 180 degrees, the deviation due to the dihedral angle is kept minimal. Utilizing this characteristic, the approximated minimum arm length can be determined, assuming that the two center axes are on the same plane. The value obtained here approaches the actual optimum as the displacement distance between the two center axes approaches zero and increases as they move farther apart.

The neighboring two profile center lines do not have matching ends. Therefore, calibration of the starting point is needed to align the starting points as closely as possible. Let each of the profile center lines, L_1 and L_2, be defined as follows:

$$L_1(d_1) = P_1 + d_1V_1, \quad L_2(d_2) = P_2 + d_2V_2 \quad (\|V_1\| = \|V_2\| = 1) \tag{13}$$

where d_1 and d_2 are the distance from P_1 and P_2; V_1 and V_2 are the trajectories of L_1 and L_2; P_1 and P_2 are the position vectors of the starting point of L_1 and L_2.

The directional vector V_s of the line L_s connecting points on L_1 and L_2 is given by:

$$V_s = L_2(d_2) - L_1(d_1) \tag{14}$$

Since the shortest length between L_1 and L_2 is simultaneously perpendicular to both L_1 and L_2, it follows that:

$$(L_2(d_2) - L_1(d_1)) \cdot V_1 = 0 \tag{15}$$

$$(L_2(d_2) - L_1(d_1)) \cdot V_2 = 0 \tag{16}$$

Using linear Equations (15) and (16), we can calculate d_1 and d_2. The closest points calculated here are the minimum distance between the profile center lines, and profiles with cross-sectional shapes require a greater clearance distance to avoid interference. From the above, the new straight lines $L_a(d_{\text{ext}})$ and $L_b(d_{\text{ext}})$ whose starting points are $L_1(d_1)$ and $L_2(d_2)$, respectively, are defined as follows:

$$L_a(d_{\text{ext}}) = L_1(d_1) + d_{\text{ext}}V_1 \tag{17}$$

$$L_b(d_{\text{ext}}) = L_2(d_2) + d_{\text{ext}}V_2 \tag{18}$$

The angle θ formed by the two straight lines is calculated as follows:

$$\theta = \arccos(V_1 \cdot V_2) \quad (\|V_1\| = \|V_2\| = 1) \tag{19}$$

The extension distance d_{ext} has the following relationship with the clearance radius r of the profile:

$$d_{\text{ext}} = \frac{r}{\tan\left(\frac{\theta}{2}\right)} = \frac{r}{\tan\left(\frac{\arccos(V_1 \cdot V_2)}{2}\right)} \tag{20}$$

Therefore, the optimal arm lengths D_1 and D_2 are defined as follows:

$$D_1 = d_1 + d_{\text{ext}}, \quad D_2 = d_2 + d_{\text{ext}} \tag{21}$$

Listing 3 calculates the closest points between two lines, lineA (L_1) and lineB (L_2), which are not necessarily coplanar. The function takes two lines, lineA (L_1) and lineB (L_2), a clearance radius r, and outputs the points A and B located on each line, respectively, adjusted for a specified arm extension.

This method has the advantage of fast computation, but it has two flaws. First, as the proximity between the two profile center lines increases, the extension length calculated here starts to exceed the optimal length. However, the proximity between the profile center lines is influenced by the dihedral angle formed by the two panels, and the impact of this angle is relatively small, as shown in Equation (12). Therefore, unless it is an extreme case, it closely approximates the actual optimal length. Second, this method assumes the cross-sectional shape of the profile as a circle. The smaller the aspect ratio of the cross-sectional shape, the greater the value it returns than the optimum value.

Listing 2. Minimum arm length using Boolean intersection volume.

```
private void RunScript(
List<Plane> frames,
Curve crossSection,
Plane orientOrigin,
double clearance,
ref object A,
ref object B,
ref object C){
  //global absolute tolerance
  Double tolerance = 0.01;

  //arm length list
  List<double> armLengths = new List<double>();

  //tangent vector list of longer of adjacent profile center−line
  List<Vector3d> adjacentVecs = new List<Vector3d>();

  //intersecting volumes
  List<Brep> intersectingVolumes = new List<Brep>();

  //create profile bounding geometry
  NurbsCurve extrusionPath = new Line(orientOrigin.Origin, orientOrigin.ZAxis, 1000).ToNurbsCurve();
  Brep profile = Brep.CreatePlanarBreps(crossSection, tolerance)[0].Faces[0].CreateExtrusion(extrusionPath,
      true);
  profile.Flip();

  for (int i = 0; i < frames.Count; i++){
    Index index = new Index(i, frames.Count);
    Brep currentProfile = profile.DuplicateBrep();
    Brep nextProfile = profile.DuplicateBrep();
    currentProfile.Transform(Transform.PlaneToPlane(orientOrigin, frames[index.currentIdx]));
    nextProfile.Transform(Transform.PlaneToPlane(orientOrigin, frames[index.nextIdx]));
    //get intersection volume between profile at i and i+1
    intersectingVolumes.Add(Brep.CreateBooleanIntersection(currentProfile, nextProfile, tolerance)[0]);
  }
  for (int i = 0; i < frames.Count; i++){
    Vector3d adjacentVec = new Vector3d();
    double armLength;
    Index index = new Index(i, frames.Count);
    //get Z Length of intersecting volume bounding box
    double lengthAtPrev = Plane.WorldXY.DistanceTo(intersectingVolumes[index.prevIdx].GetBoundingBox(
     frames[index.currentIdx]).Max);
    double lengthAtNext = Plane.WorldXY.DistanceTo(intersectingVolumes[index.currentIdx].
     GetBoundingBox(frames[index.currentIdx]).Max);

    //compare length and take larger minimum length value
    if (lengthAtPrev > lengthAtNext){
      armLength = lengthAtPrev;
      adjacentVec = frames[index.prevIdx].ZAxis;
    }
    else{
      armLength = lengthAtNext;
      adjacentVec = frames[index.nextIdx].ZAxis;
    }
    armLengths.Add(armLength);
    currentVecs.Add(frames[index.currentIdx].ZAxis);
    adjacentVecs.Add(adjacentVec);
  }
  A=armLengths;
  B=currentVecs;
  C=adjacentVecs;
}
```

Listing 3. Minimum arm length using vector equation.

```
private void RunScript(
Line lineA,
Line lineB,
double r,
ref object A,
ref object B)
{
  // Unit tangent vectors of lineA and lineB, representing directional vectors
  Vector3d u = lineA.UnitTangent;
  Vector3d v = lineB.UnitTangent;

  // Vector from the start point of lineA to the start point of lineB
  Vector3d w = lineB.From − lineA.From;

  // Calculate scalar projections of tA and tB where lines closest approach each other
  double tA = ((u ∗ v) ∗ (v ∗ w) − (u ∗ w)) / ((u ∗ v) ∗ (u ∗ v) − 1);
  double tB = ((u ∗ v) ∗ (u ∗ w) − (v ∗ w)) / (1 − (u ∗ v) ∗ (u ∗ v));

  // Points on lineA and lineB calculated using the scalar projections tA and tB
  Point3d pointOnLineA = lineA.From + (tA ∗ u);
  Point3d pointOnLineB = lineB.From + (tB ∗ v);

  // Calculate the minimum arm extension length required to avoid collisions, given the angle between lines
  double angle = Math.Acos(u ∗ v);
  double extension = r / Math.Tan(angle / 2); // Extension length calculated using the radius and half of the angle.

  // Apply the calculated extension to determine the final points A and B
  A = pointOnLineA + extension ∗ u;
  B = pointOnLineB + extension ∗ v;
}
```

4.5. Tooling and Surface Blending Clearance

The arm lengths obtained by the proposed methods (Listings 2 and 3) are the distances at which the two neighboring profiles barely intersect with one another. Additional clearance is needed where neighboring arms can achieve surface blending. This clearance serves not only the purpose of shaping for a continuous shape but also the purpose of securing tooling clearance in the assembly process (Figure 17).

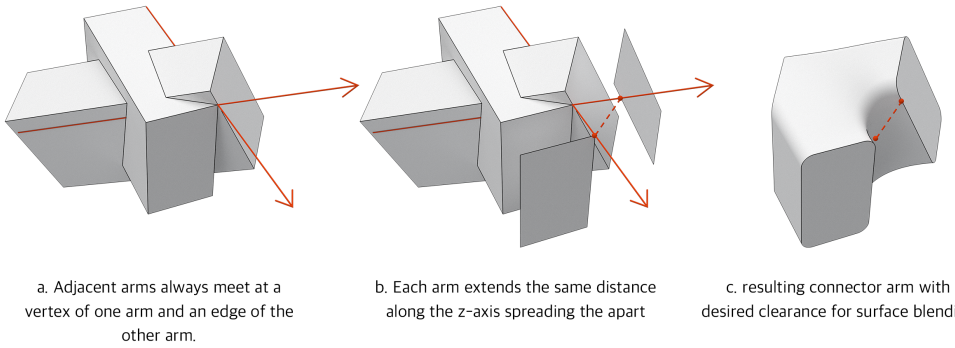

Figure 17. Arm extension for tooling clearance.

Since the two profiles are touching at this point, let the clearance distance at this time be 0, and the desired clearance distance is denoted as d_c. The additional clearance distance can be calculated using the following formula:

Given the direction unit vectors of arm A and arm B are $\vec{V}_A$ and $\vec{V}_B$ respectively, and the desired minimum clearance distance between two arms is d_c, the angle θ between $\vec{V}_A$ and $\vec{V}_B$ is calculated as:

$$\theta = \arccos\left(\vec{V}_A \cdot \vec{V}_B\right) \tag{22}$$

Let the moving distance be d_m:

$$\frac{d_c}{2} = d_m \sin\left(\frac{\arccos(\vec{V}_A \cdot \vec{V}_B)}{2}\right) \tag{23}$$

Therefore, the moving distance d_m can be calculated as:

$$d_m = \frac{d_c}{2\sin\left(\frac{\arccos(\vec{V}_A \cdot \vec{V}_B)}{2}\right)} \tag{24}$$

With the above method, the connector arm length can be optimized to automatically design a nodal connector with the minimum volume. Below are examples showing the cases where the connector arm length is uniformly applied and where it has been optimized.

Figure 18 shows a noticeable difference in volume, and the effect is particularly pronounced, especially in extreme cases. Considering the limited job box volume of a 3D printer, it can have a significant impact on packing density.

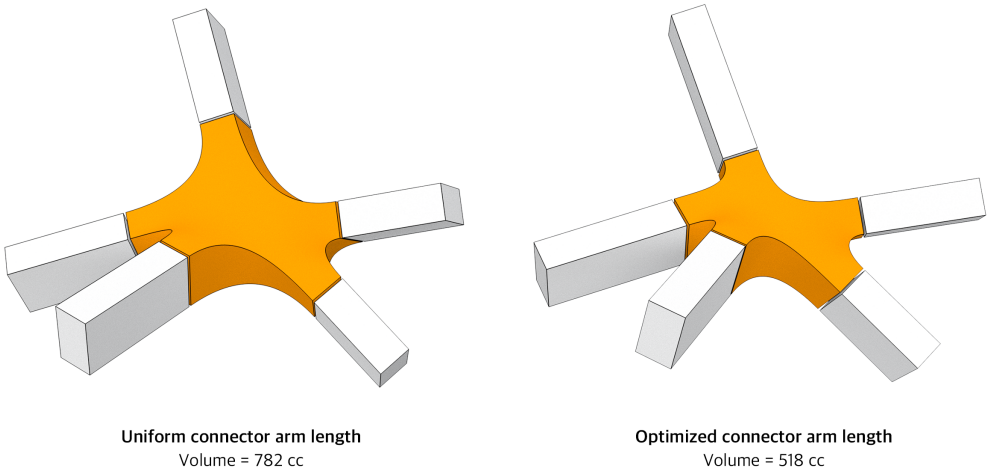

Figure 18. Difference in volume between two nodes with uniform arm length and minimum arm length.

Using the value returned from Listing 2, the additional extension length for tooling clearance, as calculated by Equation (24), can be integrated into the Rhino C# script (Listing 4).

Listing 4. C# implementation of Equation (24).

```
private void RunScript(
double clearance,
Vector3d currentVec;
Vector3d adjacentVec;
ref object A)
{

  //arm length extention for tooling clearance
  armLength += clearance / (2 * Math.Sin((Math.Acos(currentVec * adjacentVec) / 2)));
  A = armLength;
}
```

5. Results

5.1. Verification Test Mock-Up

A structure utilizing a half-scale adaptive joint system was fabricated for the purpose of testing assembly feasibility (Figures 19 and 20). To retain lightness and avoid heat shrinkage, the connector was designed as a hollow form (Figure 21).

Parts that are 3D printed in a high-temperature chamber, such as SLS (selective laser sintering), DMLS (direct metal laser sintering), and MFJ (multi-jet fusion), can encounter thermal deformation issues; therefore, the design included a maximum wall thickness of 13 mm while keeping the interior hollow. This approach is advantageous not only in terms of the print speed but it also reduces material use and weight (Figure 22).

A standard M screw tap directly embedded into a polymer material cannot withstand the required structural stress. To ensure a reliable connection between the polymer connector and the metal profile [36], dowel-nut connector detail is devised (Figure 23).

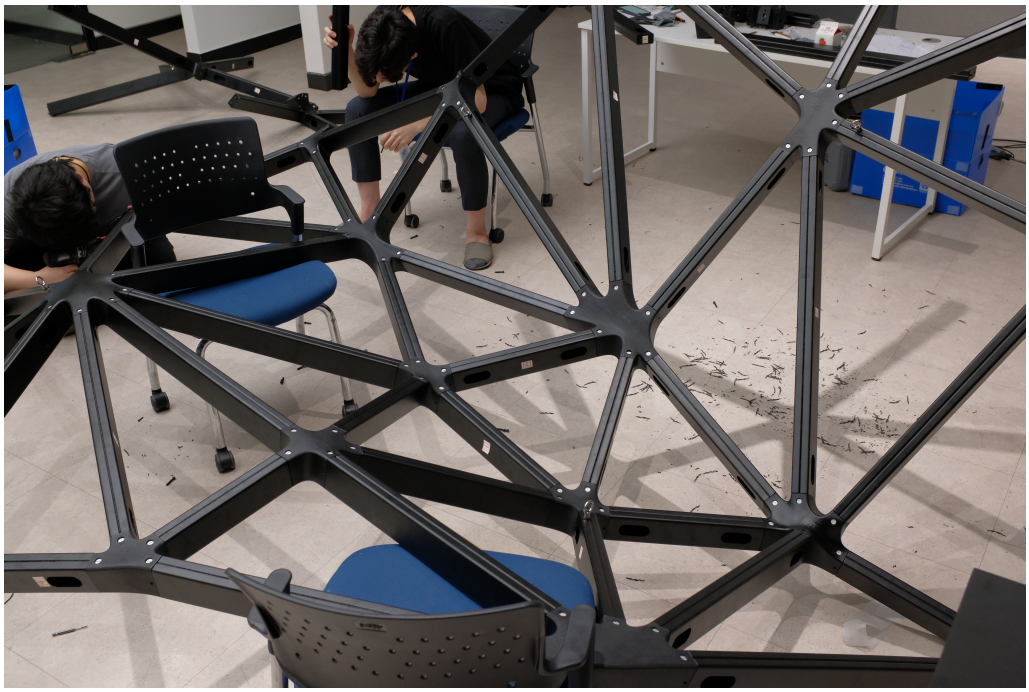

Figure 19. A 50% scale test mock-up with adaptive joint system.

Figure 20. Adaptive joint.

Figure 21. Post processing of 3D-printed parts and finished parts showing holes on each contact face for powder removal.

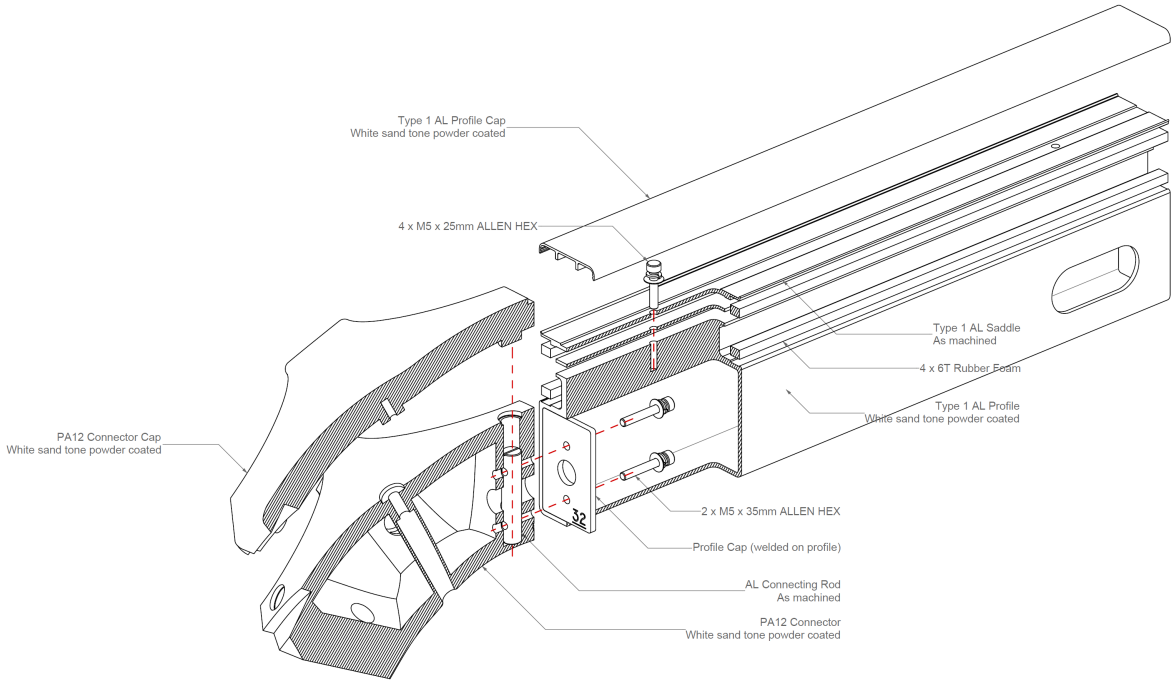

Figure 22. Cut-away assembly diagram of adaptive joint.

The tensile strength of the PA12 material used in the Hewlett-Packard Jet Fusion 4200 MJF 3D printer is 50 MPa [37], which is about 20% that of the 4000 series aluminum. In this design, the wall thickness of the aluminum profile was 2.5 mm, and the wall thickness of the PA12 (Hewlett-Packard HR PA12 GB) connector was kept at 13 mm. To prevent the tearing of the part stemming from stress concentration, all sharp edges in the design were rounded [38].

'Blobee', a dome-shaped structure resembling a deformed icosahedron with dimensions of 5 m × 5 m, was designed as a mock-up for validation that could be used as an actual living space (Figure 24). The structure was designed to eliminate the need for on-site fabrication, including welding, and was designed to allow for complete assembly by screws. The final structure is comprised of 42 units of PA12 3D-printed nodal connectors, 91 units of 50 mm × 75 mm (cross-section) 3 mm wall-thickness 6063 aluminum extrusion profiles (including the door frame), and 180 units of CNC-milled AL6061 pin connectors along with other non-structural parts (including glass panels, profiles, and nodal connector caps). For the profile-to-connector pin connection, a set of two M5 socket head screws were used, and a 70 mm × 30 mm cut-out was made for tooling entry on either end of the profile (Figures 22 and 25).

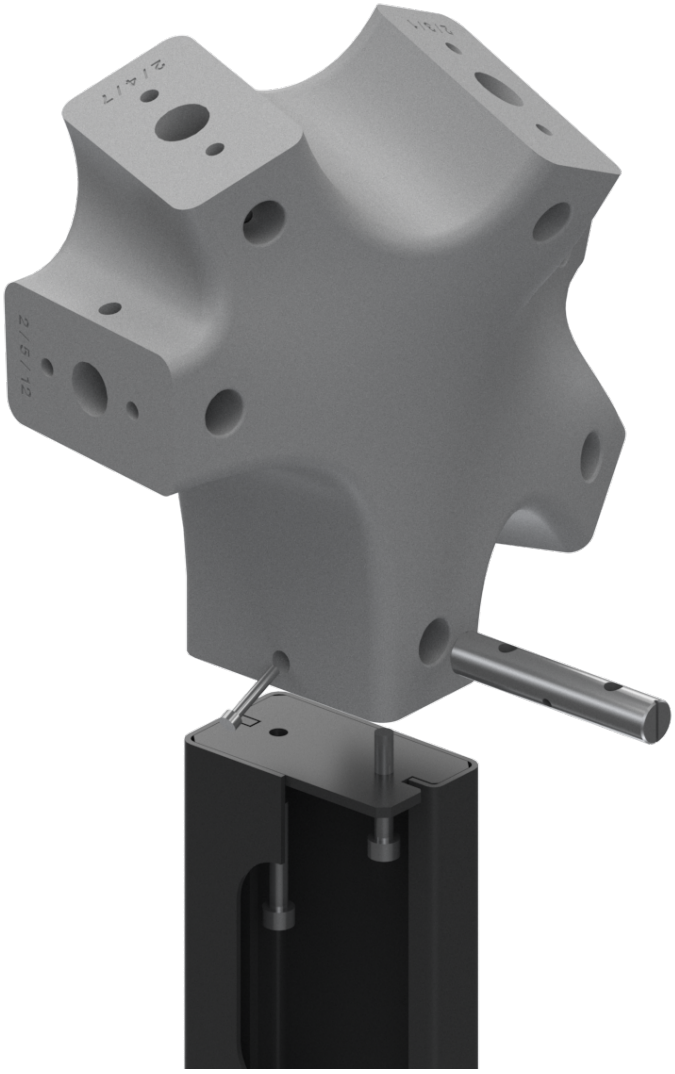

Figure 23. Assembly detail showing pin connector.

Figure 24. 'Blobee' dome-shaped adaptive joint structure.

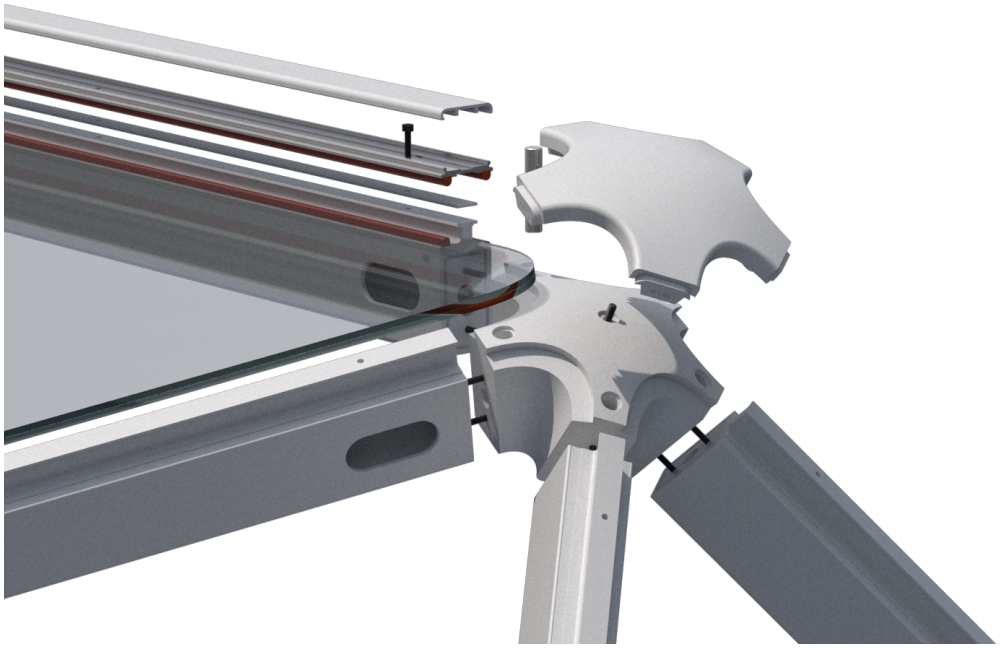

Figure 25. Assembly detail.

5.2. Finite Element Analysis

5.2.1. Analysis Setup

For LSA (linear static analysis) using the FEM (finite element method), we used a Siemens NX Nastran Solver. The following assumptions are made to simplify the analysis:

- Connector caps and profile caps are considered to have minimal impact on the structure and were excluded from the analysis model (See Figure 22).
- The connection between the profile and the glass is assumed to be well adhered to by the EVA foam weather strip, and the glue contact condition is applied.
- The steel floor structure part is excluded from the analysis model, and boundary conditions are applied to the profiles in contact with the floor structure and the M8 screws that connected them to the floor structure.

The boundary conditions for the FEA were set as follows:

- DoF 1 to 6 boundary conditions are applied to the M8 screws that connect the profiles in contact with the floor structure, fixing them to the position.
- DoF 3 to 5 boundary conditions are applied to the profiles in contact with the floor structure, restricting the Z-direction movement.

The types of elements used in the analysis are shown in Figure 26.

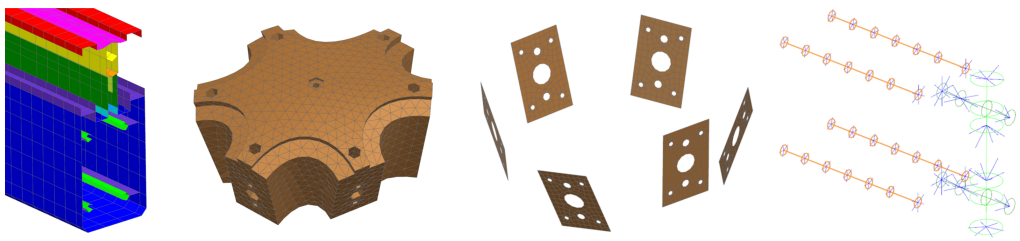

(**a**) (**b**) (**c**) (**d**)

Figure 26. Element types: (**a**) Profile: 3D 10-node tetrahedron elements; (**b**) Nodal connector: 2D 4-node quadrangle and 3-node triangle elements (mid-surface); (**c**) End cap: 2D 4-node quadrangle and 3-node triangle elements (mid-surface); (**d**) Bolt: 1D beam and RBE2 (rigid body element, type 2).

The number of elements by type is listed in Table 1.

Table 1. FE Model summary.

Element Type	Count
1D Beam	7378
Rigid Link (RBE2)	6860
Quad 4	622,684
Tri3	5707
Tetra10	307,012
Total Elements	949,641
Total Nodes	1,240,597

The material properties used in the FEA are as shown in Table 2.

Table 2. Material properties.

Part Name	Material	Elastic Modulus	Density	Poisson's Ratio	Yield Strength
Profile	AL 6063S-T5	68.90 GPa	2.70 kg/cm³	0.33	167.00 MPa
Pin	AL 6061	70.00 GPa	2.70 kg/cm³	0.33	48.00 MPa
Connector	Polyamid-12	1.80 GPa	1.01 kg/cm³	0.43	36.00 MPa
Panel	Glass	73.90 GPa	2.50 kg/cm³	0.22	-
M6 Screw	JIS S45C	205.00 GPa	7.84 kg/cm³	0.29	490.00 MPa

FEA was conducted under three unilateral load condition cases, as shown in Table 3.

Table 3. Load conditions.

Load Condition	Wind Load Direction	*X*-Axis	*Y*-Axis	*Z*-Axis
3G + 1G	x	3.0 G	0.0 G	1.0 G
	y	0.0 G	3.0 G	1.0 G
	z	0.0 G	0.0 G	4.0 G

5.2.2. FEA Result

Each case condition adds 3G of lateral load on 1G of self-weight load on the Z-axis. The deformation diagram (Figure 27) under the 4G Z-direction load condition (Table 2) shows the small deformation at the top due to the sagging of the structure (1.96 mm) and the maximum deformation at the entrance opening (3.37 mm).

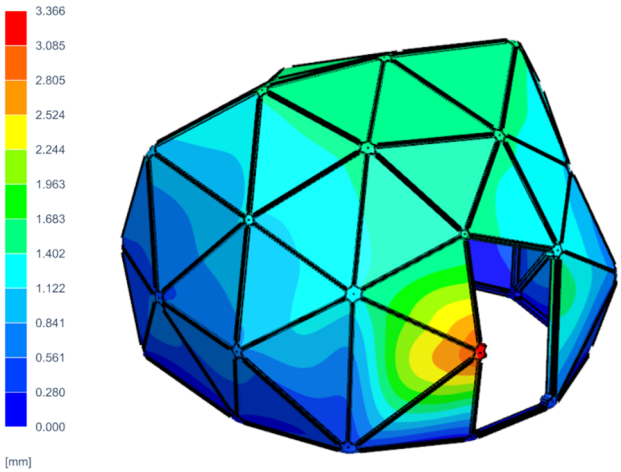

Figure 27. Deformation under Z-direction 4G load condition.

The maximum stress on the 3D-printed nodal connector occurred around the connector pin and the bolt holes, as shown in Figure 28. The maximum stress on the nodal connector was 14.90 MPa (Table 4).

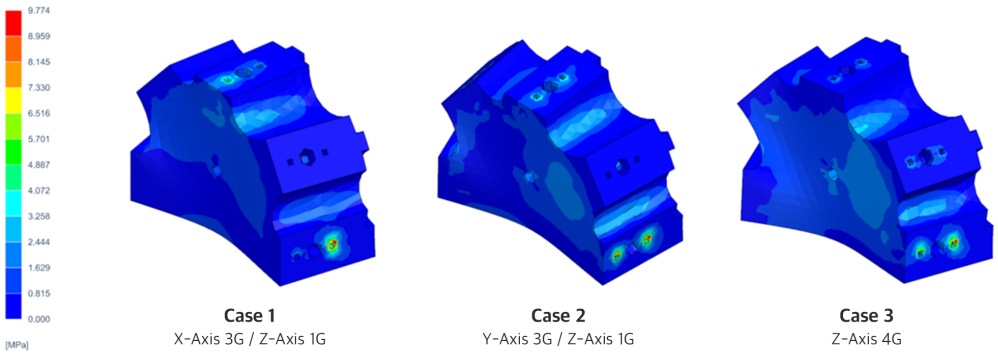

Figure 28. Stress on connector under each load conditions.

The yield strength of MJF (multi-jet fusion) 3D-printed PA12 is typically in the 35 MPa to 40 MPa range [39,40]. The FOS (factor of safety) of the nodal connector is 2.35 at minimum. Table 4 shows the FEM results on maximum stress. Given that the generally accepted FOS is 1.3, the Blobee is structurally sufficient up to the 4G condition. Contrary to expectations, the stress at the nodal connectors was not as high as expected, and the 3D-printed PA12 nodal connectors showed sufficient structural rigidity.

5.3. Test Structure Assembly

The Blobee is designed to be easily assembled and disassembled for rapid relocation to a different location. For this reason, the assembly detail of the structure was designed to exclude the use of adhesive, sealant, or welding, which would render disassembly impossible (Figure 29). Every screw hole was machine-tapped for precision and longevity.

The assembly takes three workers to finish assembly in 5 h and 3 h to disassemble (Figure 30). Assembly was slower because finding matching parts took some time. The finished structure was left for 17 days before being sent back to the workshop for minor modifications on the door part and was then reassembled on the rooftop for public use.

Table 4. FEM result of each load scenario.

		2G + 1G		**3G + 1G**		**3.5G + 1G**	
Wind Load Direction	**Part Name**	**Stress**	**FOS**	**Stress**	**FOS**	**Stress**	**FOS**
X-Axis	Profile	69.10 MPa	2.40	88.90 MPa	1.88	98.82 MPa	1.69
	Connector	-	-	**9.80 MPa**	**3.57**	-	-
	M6 Screw	54.90 MPa	8.93	72.30 MPa	6.78	84.10 MPa	5.83
	Pin	3.66 MPa	13.10	4.76 MPa	10.08	5.30 MPa	9.06
Y-Axis	Profile	84.70 MPa	1.97	113.80 MPa	1.47	161.60 MPa	1.03
	Connector	-	-	**14.90 MPa**	**2.35**	-	-
	M6 Screw	112.00 MPa	4.38	147.40 MPa	3.32	165.10 MPa	2.97
	Pin	4.81 MPa	9.98	6.33 MPa	7.58	7.09 MPa	6.77
Z-Axis	Profile	79.30 MPa	2.10	99.10 MPa	1.69	109.00 MPa	1.53
	Connector	-	-	**12.42 MPa**	**2.82**	-	-
	M6 Screw	96.60 MPa	5.07	120.70 MPa	4.06	132.80 MPa	3.69
	Pin	5.26 MPa	9.12	5.58 MPa	8.60	6.14 MPa	7.82

Figure 29. Assembly details of the Blobee.

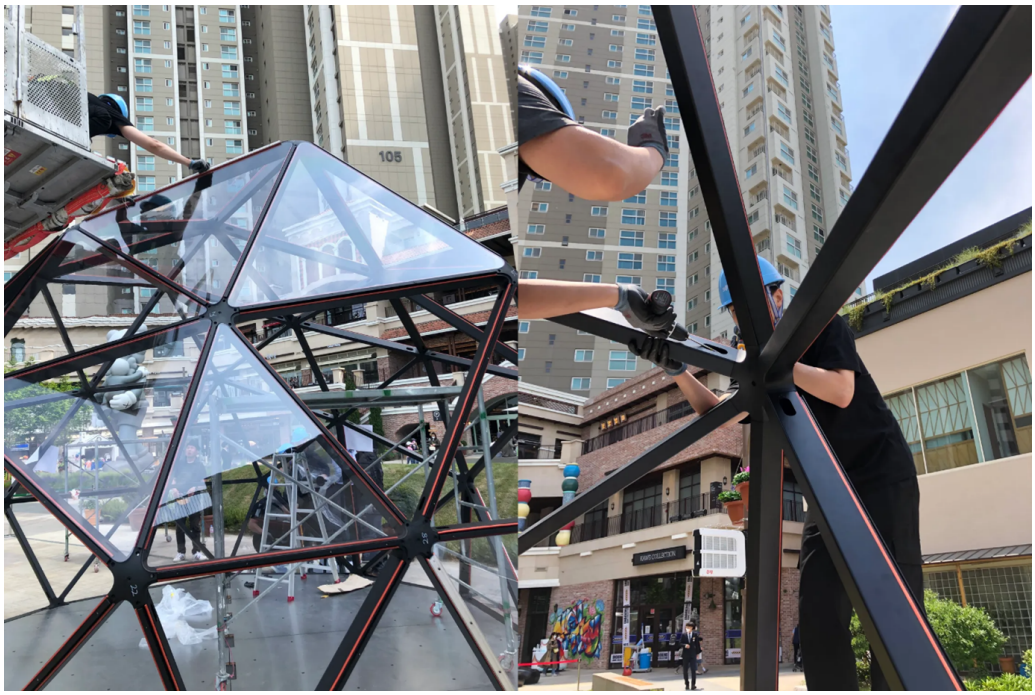

Figure 30. On-site assembly.

6. Discussion and Conclusions

This research presented detailed geometric constraints that should be considered in the triangular gridshell curtain wall structure design and provided a mathematically accurate methodology that can be applied to design automation. Furthermore, the proposed formulas were applied to automated design and validated through a physical prototype. Compared to the existing approach, which involves a large amount of volumetric computation and a complex process, it was possible to construct a simpler and more intuitive definition. Additionally, the connector arm length optimization algorithm eliminated the designer's intervention, improved work efficiency, and, most importantly, contributed significantly to the enhancement of AM productivity through minimized volume.

However, the vector equation approach among the proposed arm length optimization algorithm has limitations in that it is only valid under certain conditions, as mentioned in Section 4.4. Furthermore, the uniformly applied offsets between adjacent connector arms can occasionally lead to undesirable blended surfaces that require additional consideration and research in this aspect.

Author Contributions: Conceptualization, J.-H.A.; methodology, J.-H.A., N.-H.H. and J.-H.K.; software, J.-H.A.; validation, J.-H.A., N.-H.H. and J.-H.K.; formal analysis, J.-H.A.; investigation, J.-H.A. and N.-H.H.; resources, J.-H.A. and N.-H.H.; data curation, J.-H.A.; writing—original draft preparation, J.-H.A.; writing—review and editing, J.-H.A., N.-H.H., J.-H.K. and J.-J.K.; visualization, J.-H.A.; supervision, J.-J.K.; project administration, J.-J.K. All authors have read and agreed to the published version of the manuscript.

Funding: This research received no external funding.

Institutional Review Board Statement: Not applicable.

Informed Consent Statement: Not applicable.

Data Availability Statement: The raw data supporting the conclusions of this article will be made available by the authors upon request.

Conflicts of Interest: The authors declare no conflicts of interest.

References

1. Caetano, I.; Santos, L.; Leitão, A. Computational design in architecture: Defining parametric, generative, and algorithmic design. *Front. Archit. Res.* **2020**, *9*, 287–300. [CrossRef]
2. Tanadini, D.; Ohlbrock, P.O.; Kladeftira, M.; Leschok, M.; Skevaki, E.; Dillenburger, B.; D'Acunto, P. Exploring the potential of equilibrium-based methods in additive manufacturing: The Digital Bamboo pavilion. In Proceedings of the IASS Annual Symposia, International Association for Shell and Spatial Structures (IASS), Beijing, China, 19–22 September 2022; Volume 8, pp. 1–12.
3. Ngo, T.D.; Kashani, A.; Imbalzano, G.; Nguyen, K.T.; Hui, D. Additive manufacturing (3D printing): A review of materials, methods, applications and challenges. *Compos. Part B Eng.* **2018**, *143*, 172–196. [CrossRef]
4. Gerber, D.J. *Parametric Practices: Models for Design Exploration in Architecture*; Harvard University: Cambridge, MA, USA, 2007.
5. Woodbury, R.; Williamson, S.; Beesley, P. Prarmetric Modelling As a Design Representation in Architecture: A Process Account. In Proceedings of the Canadian Design Engineering Network (CDEN) Conference, Toronto, ON, Canada, 24–26 July 2006.
6. Sathish, K.; Kumar, S.S.; Magal, R.T.; Selvaraj, V.; Narasimharaj, V.; Karthikeyan, R.; Sabarinathan, G.; Tiwari, M.; Kassa, A.E. A comparative study on subtractive manufacturing and additive manufacturing. *Adv. Mater. Sci. Eng.* **2022**, *2022*, 6892641. [CrossRef]
7. Aish, R.; Woodbury, R. Multi-level interaction in parametric design. In Proceedings of the International Symposium on Smart Graphics, Frauenwörth Cloister, Germany, 22–24 August 2005; Springer: Berlin/Heidelberg, Germany, 2005; pp. 151–162.
8. Na, S.; Yoo, S.; Park, Y.; Park, J.; Kim, S. Study on the Connection Node System of Irregular-shaped Curtain wall Facade using 3D Printed Smart Node System. In Proceedings of the Korean Institute of Building Construction Conference, The Korean Institute of Building Construction, Seoul, Republic of Korea, 16–19 October 2018; pp. 8–9.
9. Na, S.; Lee, J.; Park, Y.; Kim, S. A Case Study of Smart Node System by using 3D Printing Technology. In Proceedings of the Korean Institute of Building Construction Conference, The Korean Institute of Building Construction, Gwangju, Republic of Korea, 20–22 October 2021; pp. 6–7.
10. Chen, T.; Lin, Y.C. Feasibility evaluation and optimization of a smart manufacturing system based on 3D printing: A review. *Int. J. Intell. Syst.* **2017**, *32*, 394–413. [CrossRef]
11. Stephan, S.; Sánchez-Alvarez, J.; Knebel, K. Reticulated structures on free-form surfaces. *Stahlbau* **2004**, *73*, 562–572. [CrossRef]
12. Grobman, Y.J.; Datta, S.; Sharman, M.; Chang, T.W.; Sweet, K. COMPUTATIONAL DESIGN in the past, present and future of digital architecture. *Autom. Constr.* **2016**, *72*, 1–2.
13. Seifi, H.; Javan, A.R.; Xu, S.; Zhao, Y.; Xie, Y.M. Design optimization and additive manufacturing of nodes in gridshell structures. *Eng. Struct.* **2018**, *160*, 161–170. [CrossRef]
14. Watson, J.; Taminger, K. A decision-support model for selecting additive manufacturing versus subtractive manufacturing based on energy consumption. *J. Clean. Prod.* **2018**, *176*, 1316–1322. [CrossRef]
15. Vayre, B.; Vignat, F.; Villeneuve, F. Designing for additive manufacturing. *Procedia CIrP* **2012**, *3*, 632–637. [CrossRef]
16. Lesage, P.; Dembinski, L.; Lachat, R.; Roth, S. Mechanical characterization of 3D printed samples under vibration: Effect of printing orientation and comparison with subtractive manufacturing. *Results Eng.* **2022**, *13*, 100372. [CrossRef]
17. Cai, C.; Tey, W.S.; Chen, J.; Zhu, W.; Liu, X.; Liu, T.; Zhao, L.; Zhou, K. Comparative study on 3D printing of polyamide 12 by selective laser sintering and multi jet fusion. *J. Mater. Process. Technol.* **2021**, *288*, 116882. [CrossRef]
18. Morano, C.; Alfano, M.; Pagnotta, L. Effect of strain rates and heat exposure on polyamide (PA12) processed via selective laser sintering. *Materials* **2023**, *16*, 4654. [CrossRef] [PubMed]
19. Dai, K.; Shaw, L. Finite element analysis of the effect of volume shrinkage during laser densification. *Acta Mater.* **2005**, *53*, 4743–4754. [CrossRef]
20. Lowke, D.; Dini, E.; Perrot, A.; Weger, D.; Gehlen, C.; Dillenburger, B. Particle-bed 3D printing in concrete construction–possibilities and challenges. *Cem. Concr. Res.* **2018**, *112*, 50–65. [CrossRef]
21. Shan, W.; Guo, L. Multi-axis NC machining of integral impeller parts based on NX. *J. Phys. Conf. Ser.* **2021**, *1885*, 022014. [CrossRef]
22. Yang, S.; Zhao, Y.F. Additive manufacturing-enabled design theory and methodology: A critical review. *Int. J. Adv. Manuf. Technol.* **2015**, *80*, 327–342. [CrossRef]
23. Manola, M.S.; Singh, B.; Singla, M.K.; Chohan, J.S.; Kumar, R.; Bisht, Y.S.; Alkahtani, M.Q.; Islam, S.; Ammarullah, M.I. Investigation of melt flow index and tensile properties of dual metal reinforced polymer composites for 3D printing using machine learning approach: Biomedical and engineering applications. *AIP Adv.* **2024**, *14*, 055016. [CrossRef]
24. Berman, B. 3-D printing: The new industrial revolution. *Bus. Horizons* **2012**, *55*, 155–162. [CrossRef]

25. Wu, P.; Wang, J.; Wang, X. A critical review of the use of 3-D printing in the construction industry. *Autom. Constr.* **2016**, *68*, 21–31. [CrossRef]
26. Shahrubudin, N.; Lee, T.C.; Ramlan, R. An overview on 3D printing technology: Technological, materials, and applications. *Procedia Manuf.* **2019**, *35*, 1286–1296. [CrossRef]
27. Lorensen, W.E.; Cline, H.E. Marching cubes: A high resolution 3D surface construction algorithm. In *Seminal Graphics: Pioneering Efforts that Shaped the Field*; Association for Computing Machinery: New York, NY, USA, 1998; pp. 347–353.
28. Huang, W.; Wu, C.; Hu, J.; Gao, W. Weaving structure: A bending-active gridshell for freeform fabrication. *Autom. Constr.* **2022**, *136*, 104184. [CrossRef]
29. Pottmann, H. Architectural geometry and fabrication-aware design. *Nexus Netw. J.* **2013**, *15*, 195–208. [CrossRef]
30. Gouraud, H. Continuous shading of curved surfaces. In *Seminal Graphics: Pioneering Efforts that Shaped the Field*; Association for Computing Machinery: New York, NY, USA, 1998; pp. 87–93.
31. Glassner, A. Building vertex normals from an unstructured polygon list. In *Graphics Gems*; Elsevier: Amsterdam, The Netherlands, 1994; pp. 60–73.
32. Max, N. Weights for computing vertex normals from facet normals. *J. Graph. Tools* **1999**, *4*, 1–6. [CrossRef]
33. Vasilchenko-Malishev, G.; Chesnokov, S. Zaryadye Park, Glass Grid Shell Roof. In Proceedings of the Challenging Glass Conference Proceedings, TU Delft, The Netherlands, 17–18 May 2018; Volume 6, pp. 671–680.
34. O'Rourke, J. Finding minimal enclosing boxes. *Int. J. Comput. Inf. Sci.* **1985**, *14*, 183–199. [CrossRef]
35. Toussaint, G.T. Solving geometric problems with the rotating calipers. *Proc. IEEE Melecon* **1983**, *83*, A10.
36. Fabbri, A.; Minghini, F.; Tullini, N. Monotonic and cyclic pull-pull tests on dowel-nut connector in laminated veneer lumber made of European beech wood. *Constr. Build. Mater.* **2022**, *359*, 129461. [CrossRef]
37. Hewlett-Packard, H. *3D Printing Materials for the HP Jet Fusion 5200 Series 3D Printing Solution-Mechanical Properties*; Technical White Paper; Hewlett-Packard: Seoul, Republic of Korea, 2020.
38. Prajapati, H.; Patel, B. Effect of curved surface of a shoulder fillet round bar on stress concentration factor for axial tension loading. *J. Kejuruter.* **2022**, *35*, 141–157. [CrossRef]
39. Hofland, E.C.; Baran, I.; Wismeijer, D.A. Correlation of process parameters with mechanical properties of laser sintered PA12 parts. *Adv. Mater. Sci. Eng.* **2017**, *2017*, 4953173. [CrossRef]
40. O'Connor, H.J.; Dickson, A.N.; Dowling, D.P. Evaluation of the mechanical performance of polymer parts fabricated using a production scale multi jet fusion printing process. *Addit. Manuf.* **2018**, *22*, 381–387. [CrossRef]